12

Electromagnetic Imaging of Biological Systems

William T. Joines, Qing H. Liu, and Gary Ybarra

CONTENTS

12.1 Introduction

Two emerging types of electromagnetic imaging are presented: electrical impedance imaging (or tomography, EIT) and microwave imaging (MWI). Both techniques rely on the contrast in electromagnetic properties (complex permittivity) of the tissues to be imaged with that of the neighboring tissue region. Both techniques use an array of sensors

around the region to be imaged. For EIT, a current due to a known voltage is passed between all electrodes within an array to determine the electrical impedance (or admittance) of the imaged tissue. For MWI, a microwave signal is sequentially transmitted through the imaged tissue to all antennas within an array to determine the scattering parameters (ratio of reflected and transmitted signals to the incident signal) of the imaged region. EIT uses a lower frequency (in the kHz or MHz range) so that the imaged region is small compared with the signal wavelength. MWI uses a higher frequency (in the GHz range) so that the imaged region is comparable to the signal wavelength. The MWI frequency is chosen to be low enough to yield an adequate depth of penetration into the imaged tissue, but high enough to allow the use of a number of small, closely spaced antennas in the array. Since antenna size is also comparable to signal wavelength, microstrip patches or waveguide apertures on high-permittivity substrates are often used to reduce the wavelength at the antenna.

Once MWI and electrical impedance imaging are fully developed for clinical use, they have great potential for the early detection of breast cancer. Other imaging methods are now available, but they have certain disadvantages that limit their acceptance as the method of choice for breast cancer screening. Magnetic resonance imaging (MRI) relies on large electrical currents in cryogenically cooled conductors to produce a strong magnetic field. Hardware and safety requirements may continue to make MRI too expensive for widespread use in breast cancer screening. X-ray imaging is now used fairly extensively, but many women dread the discomfort or pain associated with having their breast sandwiched between two hard, flat surfaces in preparation for the screening, and their aversion to this test may prevent them from participating.

For testing patients in the clinic, both MWI and EIT will most likely use the same arrangement as far as the patient is concerned. The patient will lie face down in a comfortable position on a cot or gurney, as illustrated in Figure 12.1. The breast to be screened extends into an opening containing body-temperature liquid that has approximately the same electrical properties as the normal female breast. This liquid is held within a cylindrical or rectangular thin-walled plastic container that is attached beneath the cot. For MWI, numerous small antennas are attached to the entire outer surface of the plastic container. For EIT, numerous small metal electrodes are attached on the inside surface of the plastic container so that the electrodes can flow current through the liquid and the breast tissue under test. These are the techniques, along with numerical modeling,

FIGURE 12.1
Breast imaging arrangement with patient lying comfortably face down.

that we are now using in the laboratory to obtain the results reported herein. Although we describe how we obtain the breast cancer images using phantom (artificial) tissues, we have not yet moved our imaging systems into the clinic to image breast cancer in real patients. The research and development we are now doing are necessary steps that must be taken before successful clinical applications can occur.

12.2 Development of MWI

Active MWI is an emerging technique for several biomedical imaging applications. Besides being economical and easily portable, MWI takes advantage of the high contrast in electrical properties that exists between anomalous and normal tissue over certain ranges of frequency [1–7]. Fortunately for breast cancer imaging, the contrast between normal and malignant tissue appears to be greatest over the approximate frequency range of 600 to 1000 MHz. This frequency range is both low enough and high enough to meet most of the requirements cited earlier.

While the high contrast is advantageous, it does make multiple scattering in the region more pronounced, and this adds to the difficulty of image formation. Although the specific contrasts vary with frequency, there is now a general belief that these contrasts are substantial, especially near 800 MHz (see the references cited in Refs. [8,9] and the review in Fear et al. [10]). For example, according to Joines et al. [6], at 800 MHz, the permittivity relative to air (ε_r) and the electrical conductivity (σ) for malignant breast tissue are approximately $\varepsilon_r \cong 57.2$ and $\sigma \cong 1.08$ S/m, respectively, while they are $\varepsilon_r \cong 16$ and $\sigma \cong 0.16$ S/m, respectively, for normal mammary tissue. The contrast is 3.75 for the relative permittivity and 6.75 for the electrical conductivity. Over the past few years, several research groups have been working on both hardware and software aspects of microwave breast imaging [8,9,11–15] to take advantage of the high contrast in applications of near-field MWI. The reason for the high contrast between malignant and normal tissue may be better understood through a brief examination of the frequency-dependent electrical properties of biological tissue.

12.2.1 Frequency Dependence

The frequency dependence of ε and σ is directly related to the polarization of molecules and structural interfaces caused by an applied electric field within the biological tissue. A specific polarization effect is important in determining ε and σ up to a relaxation frequency, f_r. Above this frequency the induced polarization can no longer change as fast as the applied field. Thus, above f_r the energy storage term (ε) is less, and the energy dissipation term (σ) is greater. Structural or Maxwell–Wagner relaxation, because of cellular membranes and other layered structures within the tissue, is of importance at frequencies below about 100 MHz [16]. Polar or Debye relaxation, because of the rotation of molecules or molecular groups by the applied field, is of importance in determining ε and σ at all frequencies above about 30 MHz. In the 30- to 2000-MHz range, the values of ε and σ versus frequency are highly dependent on the free-water content ($f_r \cong 25{,}000$ MHz) of the tissue. However, bound water (f_r in the 100- to 1000-MHz range) and protein molecules (f_r in the 40- to 300-MHz range) also make significant contributions to ε and σ.

Because most types of polarization can be described formally in the same qualitative manner, the Debye equations often apply very well, even though they were derived for the case of molecular rotation. For a given relaxation frequency, the Debye relations for ε and σ are [17]:

$$\varepsilon = \varepsilon_{\mathrm{H}} + \frac{\varepsilon_{\mathrm{L}} - \varepsilon_{\mathrm{H}}}{1 + \left(\frac{f}{f_{\mathrm{r}}}\right)^2} \tag{12.1}$$

and

$$\sigma = \sigma_{\mathrm{L}} + \frac{(\varepsilon_{\mathrm{L}} - \varepsilon_{\mathrm{H}})2\pi f_{\mathrm{r}}}{1 + (f_{\mathrm{r}}/f)^2} \tag{12.2}$$

where $\varepsilon = \varepsilon_{\mathrm{H}}$ at f well above f_{r} and $\sigma = \sigma_{\mathrm{L}}$, $\varepsilon = \varepsilon_{\mathrm{L}}$ at f well below f_{r}.

Two tissues having different constituencies (e.g., normal and malignant tissues) most likely will have different relaxation frequencies (f_{r1} and f_{r2}). If the operating frequency of an applied electromagnetic wave is between f_{r1} and f_{r2}, then an examination of the Debye equations shows that this is the frequency where the greatest contrast occurs between ε and σ for the two tissues [5].

12.2.2 Scattering Parameters

As stated earlier, to achieve MWI an electromagnetic wave is sequentially transmitted through the tissue region to be imaged and to all antennas within an array surrounding the region in order to determine the scattering parameters (ratio of reflected and transmitted signals to the incident signal) of the imaged region. This is important because the scattering parameters may be measured as well as calculated.

Taking just two antennas in the array, one transmitting and one receiving, the scattering parameters may be simply expressed. The electric field intensity on the transmitter side (E_1) of the region is made up of incident and reflected (scattered) components and likewise, for the electric field intensity on the receiver side (E_2) of the imaged region. This relationship is expressed as

$$E_1 = E_{1\mathrm{i}} + E_{1\mathrm{r}} \tag{12.3}$$

and

$$E_2 = E_{2\mathrm{i}} + E_{2\mathrm{r}} \tag{12.4}$$

where $E_{1\mathrm{i}}$ is a wave incident from antenna 1 into the imaged region, $E_{1\mathrm{r}}$ is reflected into antenna 1 from the region, $E_{2\mathrm{i}}$ is incident from antenna 2 into the region, and $E_{2\mathrm{r}}$ passes from the region and into antenna 2. Since the incident and scattered fields completely determine the transmitted and received signals, it is convenient to express the scattered fields as functions of the incident fields, as

$$E_{1\mathrm{r}} = S_{11}E_{1\mathrm{i}} + S_{12}E_{2\mathrm{i}} \tag{12.5}$$

and

$$E_{2\mathrm{r}} = S_{21}E_{1\mathrm{i}} + S_{22}E_{2\mathrm{i}} \tag{12.6}$$

where the scattering parameters are defined as:

$$S_{11} = E_{1r}/E_{1i}\,|_{E_{2i}=0},\ S_{12} = E_{1r}/E_{2i}\,|_{E_{1i}=0},\ S_{21} = E_{2r}/E_{1i}\,|_{E_{2i}=0},\ S_{22} = E_{2r}/E_{2i}\,|_{E_{1i}=0} \quad (12.7)$$

Thus, S_{11} is the reflection coefficient at antenna 1, under the condition that antenna 2 is terminated in the impedance of its connecting cable (usually 50 Ω), so that no signal enters the region from antenna 2. Under the same condition at antenna 2, S_{21} is the forward transmission coefficient of signals from antenna 1 to antenna 2. Likewise, S_{22} is the reflection coefficient at antenna 2, under the condition that antenna 1 is terminated in the impedance of its connecting cable (usually 50 Ω), so that no signal enters the region from antenna 1. Under the same condition at antenna 1, S_{12} is the reverse transmission coefficient of signals from antenna 2 to antenna 1.

Using the very same concepts and definitions, the scattering parameters for N antennas are expressed as

$$\begin{aligned}
E_{1r} &= S_{11}E_{1i} + S_{12}E_{2i} + S_{13}E_{3i} + \cdots + S_{1N}E_{Ni} \\
E_{2r} &= S_{21}E_{1i} + S_{22}E_{2i} + S_{23}E_{3i} + \cdots + S_{2N}E_{Ni} \\
E_{3r} &= S_{31}E_{1i} + S_{32}E_{2i} + S_{33}E_{3i} + \cdots + S_{3N}E_{Ni} \\
&\vdots \\
E_{Nr} &= S_{N1}E_{1i} + S_{N2}E_{2i} + S_{N3}E_{3i} + \cdots + S_{NN}E_{Ni}
\end{aligned} \quad (12.8)$$

12.2.3 Scattering-Parameter Imaging of Tissue Permittivity

This method of imaging relies on the propagation of electromagnetic waves into and through the region of interest as shown in Figure 12.2. The reflected and transmitted electric fields are referenced to the incident electric field to determine the magnitude and phase delay of the reflection coefficient at the nth port ($S_{nn} = |S_{nn}| \angle\phi_R = E_r/E_i$) and the transmission coefficient from port n to m ($S_{mn} = |S_{mn}| \angle\phi_T = E_t/E_i$) at multiple transmitter–receiver sites around the circumference of the region.

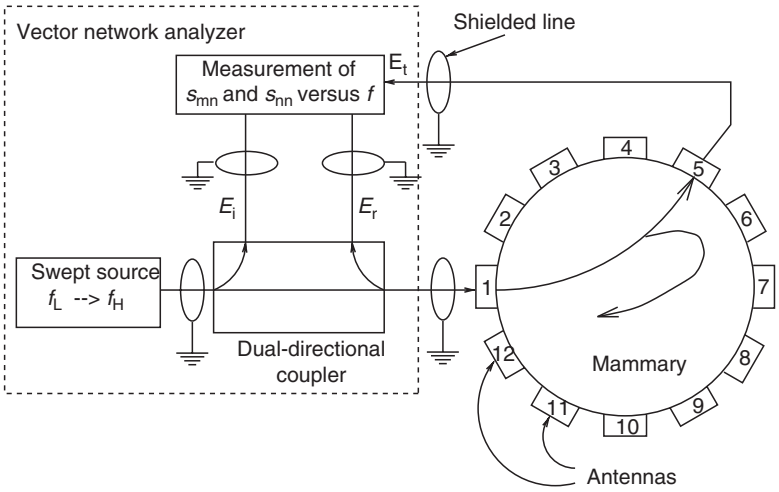

FIGURE 12.2
S-parameter measurement system.

A further visualization of the transmission–reflection method is shown in Figure 12.3, where each antenna on the circumference is a transmitter–receiver and the lines between antennas may be considered average ray paths for transmitted waves. Thus, position 1 in Figure 12.3 transmits to all other receivers at the same time and also receives reflected signals from various points within the target region. Next, position 2 transmits to all positions, and so on around the circumference. Both the amplitude and phase delay of transmitted and reflected signals are functions of the complex permittivity that the particular ray path encounters in traversing or partially traversing the normal and malignant breast tissue regions. The data collected with this method are processed by computer to produce images of subregions of differing permittivity and conductivity within the mammary tissue.

At present, we use a vector network analyzer (HP 8753A, 0.3 MHz to 3 GHz) to perform the measurement functions in Figure 12.2. In a fully developed MWI system, the network analyzer will be replaced with lower-cost, application-specific, individual components.

As an example to illustrate the transmission–reflection imaging method, we use a simplified multiport network theory; a more rigorous full-wave theory will be summarized in Section 12.4. Let d be the distance of an average ray path from a transmitter at port 1 to a receiver at port 7 in Figure 12.3, let Z_0 be the receiver or transmitter impedance, and let Z_M be the intrinsic impedance that the rays encounter in the bulk tissue between transmitter and receiver. From two-port network theory, the reflection coefficient (S_{11}) looking from the transmitter antenna into the bulk tissue is

$$S_{11} = \frac{(Z_M^2 - Z_0^2)\tanh \gamma d}{2Z_0 Z_M + (Z_M^2 - Z_0^2)\tanh \gamma d} = \frac{E_r}{E_i} \tag{12.9}$$

and the transmission coefficient (S_{71}) from port 1 to port 7 is

$$S_{71} = \frac{2Z_0 Z_M \sqrt{1 - \tanh^2 \gamma d}}{2Z_0 Z_M + (Z_M^2 - Z_0^2)\tanh \gamma d} = \frac{E_t}{E_i} \tag{12.10}$$

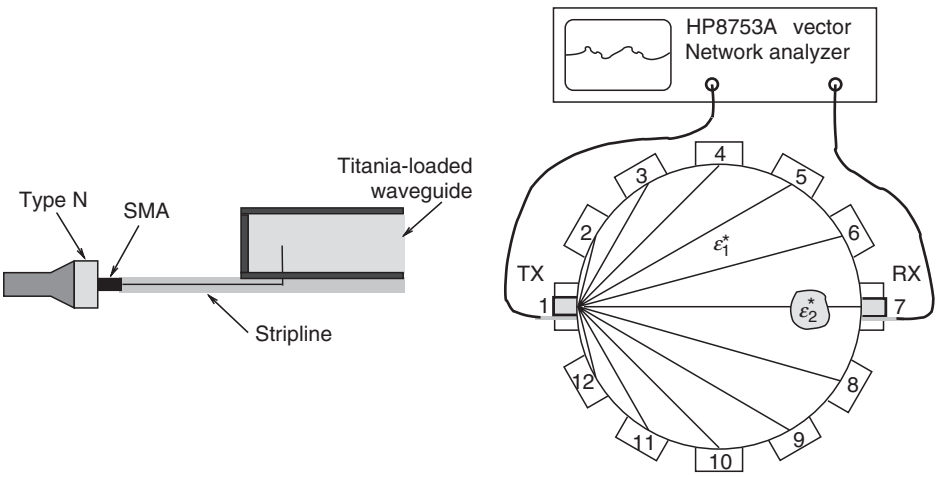

FIGURE 12.3
Top view of the cylindrical plastic container showing some of the antennas in the total array.

where $\gamma = j\omega\sqrt{\mu_0\varepsilon^*}$ is the propagation constant of the bulk tissue, and $\omega = 2\pi f$, where f is the frequency in hertz. Let $Z_M = \sqrt{\mu_0/\varepsilon^*} = 377/\sqrt{\varepsilon_r^*}$ and $Z_0 = 50\ \Omega$, then $Z_0/Z_M = \sqrt{\varepsilon_r^*}/7.54$, and S_{11} and S_{71} become

$$S_{11} = \frac{(56.85 - \varepsilon_r^*)j\tan\left(2\pi f\sqrt{\varepsilon_r^*}d/c\right)}{15.08\varepsilon_r^* + (56.85 + \varepsilon_r^*)j\tan\left(2\pi f\sqrt{\varepsilon_r^*}d/c\right)} = \frac{E_r}{E_i} \tag{12.11}$$

$$S_{71} = \frac{15.08\sqrt{\varepsilon_r^*}\sqrt{1 - j\tan^2\left(2\pi f\sqrt{\varepsilon_r^*}d/c\right)}}{15.08\varepsilon_r^* + (56.85 + \varepsilon_r^*)j\tan\left(2\pi f\sqrt{\varepsilon_r^*}d/c\right)} = \frac{E_t}{E_i} \tag{12.12}$$

where $c = 3 \times 10^8$ m/s. For example, if $d = 0.1$ m, $f = 800$ MHz, and the measured values are

$$S_{11} = 0.200\angle 81.76^\circ = -13.94\,\text{dB}\angle 81.76^\circ \tag{12.13}$$

$$S_{71} = 0.011\angle 86.49^\circ = -39.17\,\text{dB}\angle 86.49^\circ \tag{12.14}$$

then the complex permittivity of the bulk tissue medium at $f = 800$ MHz is determined as

$$\varepsilon_r^* = 36 - j36 = \frac{\varepsilon}{\varepsilon_0} - j\frac{\sigma}{\omega\varepsilon_0} \tag{12.15}$$

where $\varepsilon = 36\varepsilon_0$ and $\sigma = 1.60$ S/m. From our previous measurements [6], normal mammary tissue at 800 MHz would yield $\varepsilon_r^* = 17 - j4$, or $\varepsilon = 17\varepsilon_0$ and $\sigma = 0.18$ S/m. Thus, $\varepsilon_r^* = 36 - j36$ would represent a very large difference in expected tissue properties along the path from port 1 to port 7, which passes through the region occupied by ε_2^* in Figure 12.3. This example is intended to illustrate how the contrast in complex permittivity of a region can not only be measured but also located by coordinate position.

12.2.4 Power, Signal Attenuation, and Signal-to-Noise Ratio

At an operating frequency of 800 MHz, the free space wavelength is $\lambda_0 = 37.5$ cm. In normal breast tissue the wavelength is reduced to $\lambda_{\text{normal}} = \frac{\lambda_0}{\sqrt{\varepsilon_r}} = 9.375$ cm, assuming that the dielectric constant is 16 for normal breast tissue. The distance between any pair of transmitting and receiving antennas is less than 20 cm. Therefore, all measurements are made within a region comparable to the wavelength. The propagation loss between transmitting and receiving antennas is typically in the range of 8 to 16 dB. A typical dielectrically loaded waveguide antenna used for MWI has a 3×3 cm aperture. If the transmitting antenna is operated at a transmitted power of 0 dB m or 1 mW, it results in a transmitted power density of 0.11 mW/cm^2, nine times below the ANSI safety level. The received power is -16 to -8 dB m or 25 to 158 μW. The scattered signal from the tumor is typically 0.01% of of the incident wave. Since the network analyzer's noise level is approximately -90 dB m, the signal-to-noise ratio (SNR) at the receiving antenna is on the order of 30 dB.

12.3 Three-Dimensional Formulation

Currently, there are few methods developed for MWI in three dimensions because of the large computational demand in both forward and inverse problems of inhomogenous media. While two-dimensional (2-D) and 3-D imaging techniques based on the scalar-wave approximation have been developed with some success, breast cancer imaging is inherently a 3-D problem and requires the full 3-D inverse scattering algorithms based on the vectorial Maxwell's equations. In our imaging research we have developed a fast inverse scattering method based on the combination of the contrast source inversion and the fast Fourier transform (FFT) algorithms.

Because of the volumetric inhomogeneities in biological tissues, surface integral equation methods become impractical. Methods based on volumetric techniques are more appealing. We focus on the frequency-domain solution of a volume integral equation (VIE) for inhomogenous media. In a typical inhomogenous tissue medium, both the forward and the inverse scattering problems can be formulated using VIEs. The conventional forward scattering method for VIEs is the method of moments (MoM) [18], but the computational cost is prohibitively high; several 3-D forward problems have been solved in a number of articles [19–22] using this approach. If the VIE involves N unknowns, the MoM has a memory requirement of $O(N^2)$, and a CPU time requirement of $O(N^2)$ or $O(N^3)$ depending on whether the resulting matrix equation is solved iteratively or by direct inversion.

An important improvement over the MoM is a variant of Bojarski's k-space method (see references in Ref. [23]), the so-called conjugate-gradient fast Fourier transform (CG-FFT) method proposed during the 1980s [24,25], which uses iterative the Krylov subspace method [26] combined with FFT or nonuniform FFT [27]. Zhang and Liu [28] recently developed a biconjugate-gradient FFT method based on the weak-form discretization of Zwamborn and van den Berg and showed a significant improvement over the CG-FFT method for wave scattering problems. This method has been further accelerated by the stabilized biconjugate-gradient fast Fourier transform (BCGS-FFT) method for wave scattering by Xu et al. [29]. Recently, the adaptive integral method developed for surface integral equations [30] has been further developed for VIEs to accelerate MoM by using two sets of basis functions to represent near-field and far-field interactions [31].

In the present work, we apply the BCGS-FFT method to MWI by solving the VIE. The problem under consideration is schematically shown in Figure 12.4, where an arbitrary

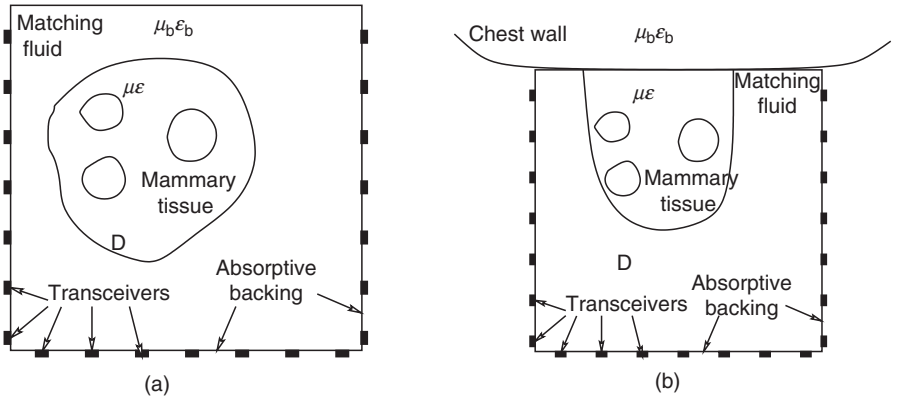

FIGURE 12.4
Imaging chamber from above (a) and from the side (b).

number of antennas are mounted on the plastic container surrounding the phantom model of breast tissue. Specific configurations for simulation will be described in a later section. We calculate the electromagnetic fields both inside the tissue medium and at the receiver array for any source locations. For MWI of breast tissue, the excitation sources (antennas) are in the near-field zone, and the incident field cannot be approximated as a plane wave. Therefore, we include the effects of the finite sources in the near-field zone.

In the following section, we derive from the vectorial Maxwell's equations the VIE for 3-D MWI in the discretized form that we use. Iterative methods for the solution of this discretized linear system are then described. Numerical results are shown to validate the method for MWI.

12.4 Wave Equation and VIE

From Maxwell's equations with an assumed time dependence $e^{j\omega t}$,

$$\nabla \times \mathbf{E} = -j\omega\mu\mathbf{H} \tag{12.16}$$

$$\nabla \times \mathbf{H} = (\sigma + j\omega\varepsilon)\mathbf{E} + \mathbf{J} = j\omega\left(\varepsilon - j\frac{\sigma}{\omega}\right)\mathbf{E} + \mathbf{J} = j\omega\varepsilon^*\mathbf{E} + \mathbf{J} \tag{12.17}$$

$$\nabla \cdot \mathbf{D} = \rho \tag{12.18}$$

$$\nabla \cdot \mathbf{B} = 0 \tag{12.19}$$

we may let

$$\mathbf{B} = \nabla \times \mathbf{A} \tag{12.20}$$

since $\nabla \cdot \nabla \times \mathbf{A} \triangleq 0$ maintains $\nabla \cdot \mathbf{B} = 0$, where $\mathbf{A}$ is the vector potential. Substituting Equation 12.20 into Equation 12.16 yields

$$\nabla \times \mathbf{E} = -j\omega(\nabla \times \mathbf{A}) \tag{12.21}$$

or

$$\nabla \times (\mathbf{E} + j\omega\mathbf{A}) = 0 \tag{12.22}$$

Since $\nabla \times (\nabla\phi) \triangleq 0$, we may let the term in parentheses in Equation 12.22 be the negative gradient of the scalar potential ϕ, and express $\mathbf{E}$ as

$$\mathbf{E} = -\nabla\phi - j\omega\mathbf{A} \tag{12.23}$$

Note that if $\omega = 0$, then $\mathbf{E} = -\nabla\phi$, as expected for static fields. We now invoke the Lorenz condition, which defines the divergence of $\mathbf{A}$ as

$$\nabla \cdot \mathbf{A} = -j\omega\mu\varepsilon^*\phi \tag{12.24}$$

Substituting this condition into Equation 12.23 yields

$$\mathbf{E} = -\mathrm{j}\omega\left[1 + \frac{\nabla\nabla\cdot}{k^2}\right]\mathbf{A} \tag{12.25}$$

where $k^2 = \omega^2\,\mu\varepsilon^*$. Since $\mathbf{E}$ and $\mathbf{H}$ are propagating field intensities that satisfy a wave equation, then $\mathbf{A}$ must satisfy a wave equation obtained as follows. Substitute Equation 12.20 and Equation 12.23 into Equation 12.17 to yield

$$\nabla \times \nabla \times \mathbf{A} \triangleq \nabla(\nabla \cdot \mathbf{A}) - \nabla^2\mathbf{A} = \mathrm{j}\omega\mu\varepsilon^*(-\nabla\phi + \mathrm{j}\omega\mathbf{A}) + \mu\mathbf{J} \tag{12.26}$$

or (again using the Lorenz condition),

$$\nabla^2\mathbf{A} = -\omega^2\mu\varepsilon^*(\mathbf{r})\mathbf{A} - \mu\mathbf{J} \tag{12.27}$$

A solution to Equation 12.27 is in general not available in a closed form because $\varepsilon^*(\mathbf{r})$ is inhomogenous. However, for a homogenous medium with constant complex permittivity ε_b^*, one can find the solution in closed form

$$\mathbf{A}^{\mathrm{inc}}(\mathbf{r}) = \mu\int_V \mathbf{J}(\mathbf{r}')g(\mathbf{r},\mathbf{r}')\,\mathrm{d}V' \tag{12.28}$$

where $\mathbf{r}$, $\mathbf{r}'$, and $\mathbf{R} = \mathbf{r} - \mathbf{r}'$ are vectors from the origin to the field point, from the origin to the source point, and from the source point to the field point, respectively. Green's function in Equation 12.28 for the homogenous medium is given by $g(\mathbf{r},\mathbf{r}') = \mathrm{e}^{-\mathrm{j}k_b R}/4\pi R$, where $k_b = \omega\sqrt{\mu\varepsilon_b^*}$ is the complex wavenumber of the medium. We call this solution $\mathbf{A}^{\mathrm{inc}}$, the vector potential for the incident field in a homogenous background medium. The corresponding incident electric field can be found from Equation 12.25 as

$$\mathbf{E}^{\mathrm{inc}} = -\mathrm{j}\omega\left[1 + \frac{\nabla\nabla\cdot}{k_b^2}\right]\mathbf{A}^{\mathrm{inc}} \tag{12.29}$$

For an inhomogenous medium, even though a closed form solution is not available, one can express the solution in terms of an integral equation through the equivalence principle, as discussed below.

In order to introduce the equivalence principle, the key is to rewrite Maxwell's equations into a second-order partial differential equation for the electric field:

$$\nabla^2\mathbf{E} + k_b^2\mathbf{E} = \mathrm{j}\omega\mu[\mathbf{J} + \mathbf{J}_{\mathrm{eq}}] \tag{12.30}$$

where

$$\mathbf{J}_{\mathrm{eq}} = \mathrm{j}\omega[\varepsilon^*(\mathbf{r}) - \varepsilon_b]\mathbf{E} \tag{12.31}$$

is the volume equivalent electric current density induced in the inhomogenous medium.

Thus, from Equation 12.30, the total field $\mathbf{E}$ can be written as the superposition of the incident field $\mathbf{E}^{\mathrm{inc}}$ due to the primary source $\mathbf{J}$ and the scattered field $\mathbf{E}^{\mathrm{sct}}$ due to the induced source $\mathbf{J}_{\mathrm{eq}}$. Similar to the incident vector potential and incident electric field, the scattered vector potential and scattered electric fields are

$$\mathbf{A}^{\text{sct}}(\mathbf{r}) = \mu \int_V \mathbf{J}_{\text{eq}}(\mathbf{r}')g(\mathbf{r}, \mathbf{r}')\,\mathrm{d}V' \tag{12.32}$$

$$\mathbf{E}^{\text{sct}} = -\mathrm{j}\omega\left[1 + \frac{\nabla\nabla\cdot}{k_{\text{b}}^2}\right]\mathbf{A}^{\text{sct}} \tag{12.33}$$

The total electric field **E(r)** is composed of an incident field plus a scattered field, and it is the scattered field that we need to determine. Thus, combining Equation 12.31 through Equation 12.33, we have

$$\mathbf{E}(\mathbf{r}) - \mathbf{E}^{\text{inc}} = \omega^2\mu\left(1 + \frac{\nabla\nabla\cdot}{k_b^2}\right)\int_V \mathbf{E}(\mathbf{r}')g(\mathbf{r}, \mathbf{r}')[\varepsilon^*(\mathbf{r}') - \varepsilon_b^*]\,\mathrm{d}V' \tag{12.34}$$

where the subscript b denotes a parameter of the background medium (normal tissue and liquid with the same properties). Equation 12.34 is the integral equation representation of the scattered electric field everywhere in space. In particular, for $\mathbf{r} \in V$, Equation 12.34 is a Fredholm integral equation of the second kind. This is the integral equation we solve for the internal electric field **E** for $\mathbf{r} \in V$, from which the field everywhere in the region can be obtained. This type of VIE has been solved by using the MoM [18,20,21]. In our work we will use an alternative discretization method coupled with the Krylov subspace iterative technique to significantly speed up the numerical solution of the problem.

12.4.1 Microwave Imaging

In MWI, scattering parameters are measured using the antennas mounted on the surface of the plastic container in Figure 12.4. The objective of MWI is to reconstruct the distribution of the complex permittivity inside the tissue given the measured scattering parameters.

First, for the MWI system design optimization, the forward problem must be solved. This is to calculate the electric field distribution, given a set of antennas and known distribution of the complex permittivity. In the general problem of microwave interaction with a tissue medium shown in Figure 12.4, an inhomogenous medium with a finite volume V is embedded in an isotropic, homogenous background medium with constant permittivity ε_b, electric conductivity σ_b, and permeability μ_b. This background medium may be air or a matching fluid that is designed to approximately match the electrical properties of the tissue to enhance the SNR in the measurement of the scattered field [9]. The inhomogenous volume V is characterized by nonuniform distributions of permittivity $\varepsilon(\mathbf{r})$ and conductivity $\sigma(\mathbf{r})$; and permeability is assumed constant, that is, $\mu = \mu_b$. The objective is to solve for the electric field everywhere in space due to a finite antenna (usually electrically small because a large array of antennas is needed in an array imaging system). For more details of the BCGS-FFT method, the reader is referred to Refs. [9,28,29,32].

The above discussion is for the forward problem where the distribution of the complex permittivity is known. In reality, for the clinic application of MWI and electrical impedance tomography, we need to solve the inverse scattering problem where the complex permittivity is an unknown distribution. From some limited measurement data collected on the surface of the container, we infer such unknown permittivity distribution by solving the inverse problem through Equation 12.34. In our work, we apply both the distorted Born iterative method and the contrast source inversion method to solve this inverse problem. For details of such inverse solvers, the reader is referred to Refs. [9,33–35].

12.4.2 Electrical Impedance Tomography

This imaging method uses multiple planar electrodes positioned around the region to be imaged, as in Figure 12.5. Impedance or admittance measurements are made between all electrodes, two at a time. Thus, in a parallel-plate capacitor sense, the admittance between any pair of electrodes is the ratio of current to voltage as:

$$Y = \frac{I}{V} = \frac{\int_S \mathbf{J} \cdot d\mathbf{S}}{\int_0^d \mathbf{E} \cdot d\mathbf{l}} = \frac{\int_S (\sigma + j\omega\varepsilon)\mathbf{E} \cdot d\mathbf{S}}{\int_0^d \mathbf{E} \cdot d\mathbf{l}} = (\sigma + j\omega\varepsilon)\frac{A}{d} = j\omega\varepsilon^* \frac{A}{d} \tag{12.35}$$

or $Y = G + j\,\omega C$, where $G = \sigma\,(A/d)$, $C = \varepsilon\,(A/d)$, and $\varepsilon^* = \varepsilon - j\,\frac{\sigma}{\omega}$ is the measured complex permittivity if A/d is known from calibration data. The real and imaginary parts of ε^*, the permittivity ε, and the conductivity σ are the electrical properties of the composite tissue between pairs of electrodes. The factor (A/d) is an effective area-to-distance ratio that may be different for each electrode pair, but this ratio is determined by measuring a material with known electrical properties (such as 0.15 M NaCl at 24°C).

In general, the electric field will be nonuniform but most intense in the region between the electrode pair selected for measurement. The fields between adjacent electrodes will measure properties near the tissue surface, while more diametrically opposed electrodes will measure the composite properties across the tissue region. Such a sequence of measurements is stepped around to include all electrode pairs surrounding the region in 3-D, so that the next set of measurements would be between electrode 2 and all the other electrodes, and so on. Thus, the mapping and imaging of a region are done based on the differing electrical properties within the region.

Impedance imaging is a subject that has been under continuing investigation [36–40]. Research into impedance imaging in our research group began in 1975. We used an open-ended coaxial probe that produced a nonradiating, fringing field to measure the admittance of the material against which the probe was held. This was essentially a two-electrode system that measured the admittance between the inner and outer conductors as given in Zhang and Liu [35]. Moving this noninvasive probe to different positions on the surface of the body, we were able to locate and map out the tumors lying near the skin surface on the bodies of two cancer patients. This work indicated that even

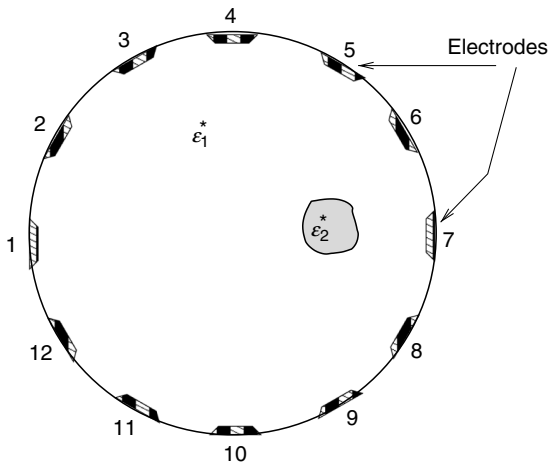

FIGURE 12.5
Configuration of electrical impedance tomography.

when measured through the intact skin, cancerous tissue generally has greater electrical conductivity and permittivity than normal surrounding tissue [41].

The forward and inverse problems of EIT can also be formulated in the same way as for the MWI, that is, using the volume integral Equation 12.34. This is especially convenient if the electrodes are small and can be considered as point electrodes. For finite-size electrodes, in order to apply the boundary conditions on the electrode surface, we use the high-order finite element and spectral element methods to solve the partial differential equations directly in the forward problem. For the inverse problem, we use the distorted Born iterative method [42,43].

12.5 Three-Dimensional Images Reconstructed from Simulated Three-Dimensional MWI Data

Figure 12.6 shows the measurement setup to image two identical spherical anomalies both with $\varepsilon_r = 48$ and $\sigma = 0.8$. The sources and receivers are evenly distributed over the six surfaces of the cuboid. The two spheres of radius 1.1 cm are located at (3.9,0,0) and (−3.9,0,0) cm, respectively. The imaged domain is discretized into $31 \times 31 \times 31$ voxels. The reconstructed ε_r and σ are displayed on three orthogonal slices in Figure 12.7, showing a high fidelity to the ground truth.

12.6 Two-Dimensional Images Reconstructed from Measured Two-Dimensional EIT Data

This section presents three examples of images reconstructed from measured data obtained from a Two-Dimensional EIT system.

12.6.1 Case 1: One Insulator Object Inside the Container

The first example is Case 1, shown in the left panel of Figure 12.9. The difference between the total field and the background field in the right panel of Figure 12.9 is the measured

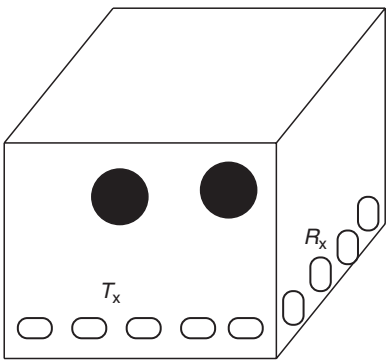

FIGURE 12.6
The setup of Three-Dimensional imaging of two spherical anomalies separated by 7 cm.

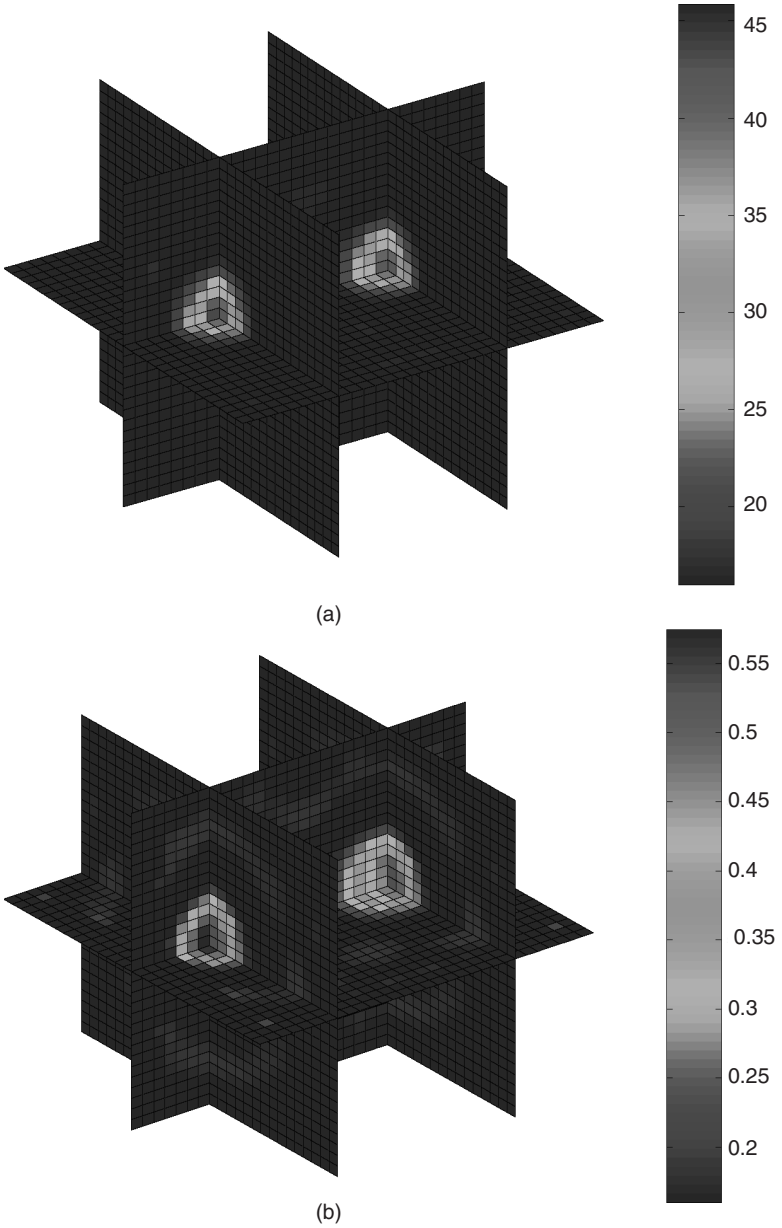

FIGURE 12.7 (See color insert following page 380.)
Inversion for Figure 12.6 on three orthogonal slices through the center of the anomalies. Inverted dielectric constant ε_r (a) and conductivity σ (b).

secondary field. The reconstructed image from this secondary field is shown in the left panel of Figure 12.8. The dotted circle in this figure indicates the ground truth of the object. It is observed that the reconstructed image matches well with the ground truth, although the absolute values of the conductivity of the highly resistive object are not well recovered because of the extreme contrast.

In order to show the misfit between the reconstructed data and the measured data, we take the reconstructed 2-D conductivity map in the left panel of Figure 12.8 and use the

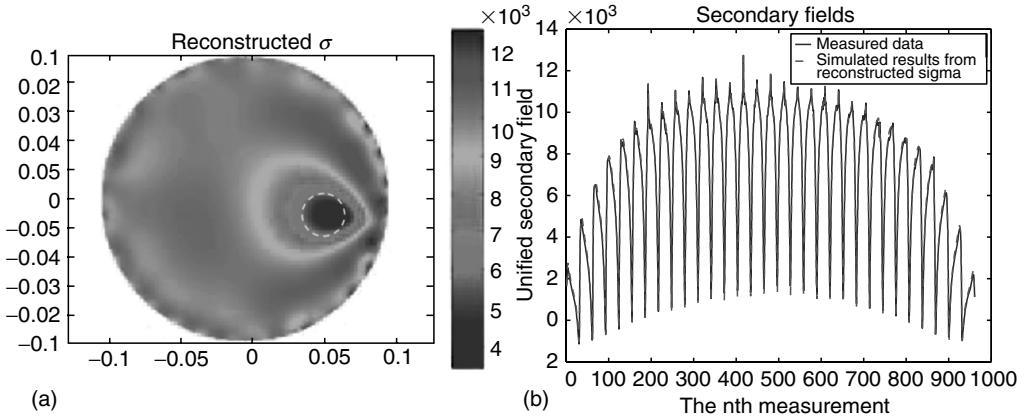

FIGURE 12.8 (See color insert following page 380.)
Left: Image reconstructed from the measured data in Case 1. The dashed circle indicates the ground truth. Right: Comparison of the secondary field between measurements and simulated by forward solver with the reconstructed σ in Case 1.

forward simulator to predict the data corresponding to this image. The comparison between the measured data (blue curve) and the simulated data (red curve) using the reconstructed image is shown in the right panel of Figure 12.8. We observe that these two sets of results have excellent agreement, indicating small data misfit from the reconstructed data.

12.6.2 Case 2: Two Insulator Objects Inside the Container

The setup of the second example (Case 2) is shown in the left panel of Figure 12.10. It is similar to Case 1, except that two insulators (beakers) are inserted into the container. The measured total field and background field are shown in the right panel of Figure 12.10. From the secondary field, the distorted Born iterative method (DBIM) reconstructs the

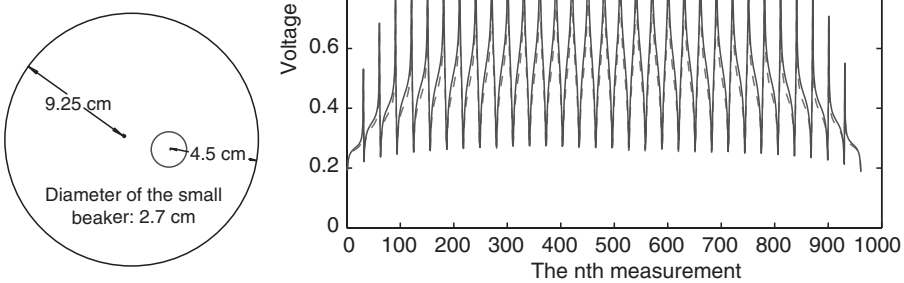

FIGURE 12.9
Left: The setup of Case 1 with one insulator object (beaker). Right: The measured voltage with and without the object in Case 1.

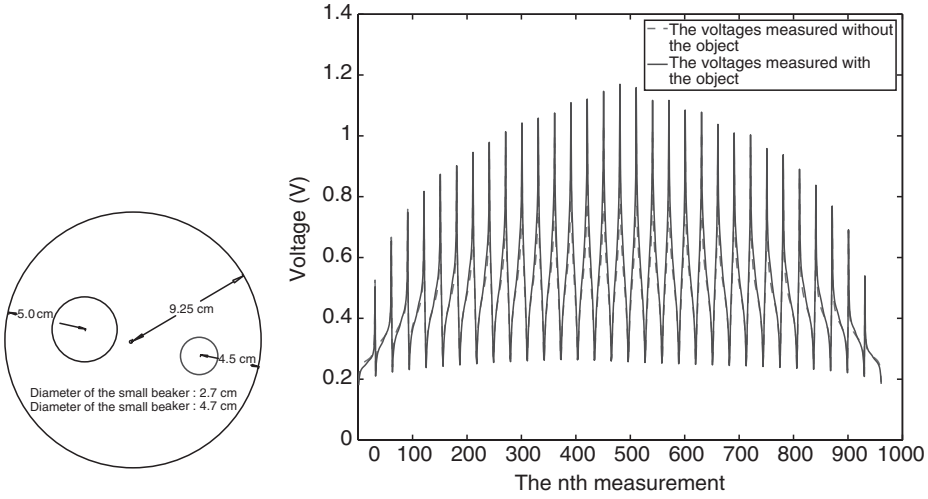

FIGURE 12.10
Left: The setup of Case 2 with two nonconducting circular objects (beakers). Right: The measured voltage with and without the objects in Case 2.

image shown in the left panel of Figure 12.11. The dotted circles in this figure indicate the ground truth of the objects. It is observed that the reconstructed image matches well with the ground truth, although the absolute values of the conductivity of the highly resistive objects are again not well recovered because of the extreme contrasts.

From the reconstructed conductivity image, we use the forward simulator to predict the secondary field data. This simulated result is then compared with the measured secondary field in the right panel of Figure 12.11. Again, we observe that these two sets of results have excellent agreement, indicating small data misfit from the reconstructed data.

12.6.3 Case 3: One Conductive and One Resistive Object Inside the Container

The third case, shown in the left panel of Figure 12.12, consists of two objects in the container. The bigger object is a conductive metal cylinder, while the smaller

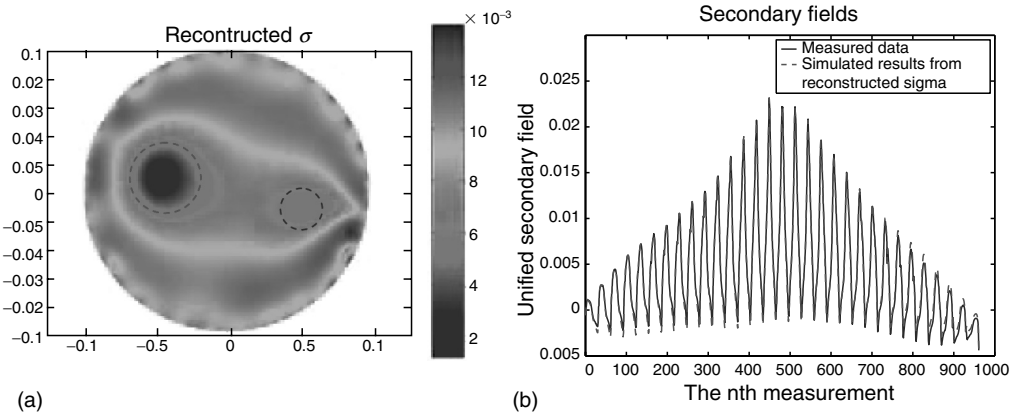

FIGURE 12.11 (See color insert following page 380.)
Left: Image reconstructed from the measured data in Case 2. The dashed circles indicate the ground truth. Right: Comparison of the secondary field between measurements and simulated by forward solver with the reconstructed σ in Case 2.

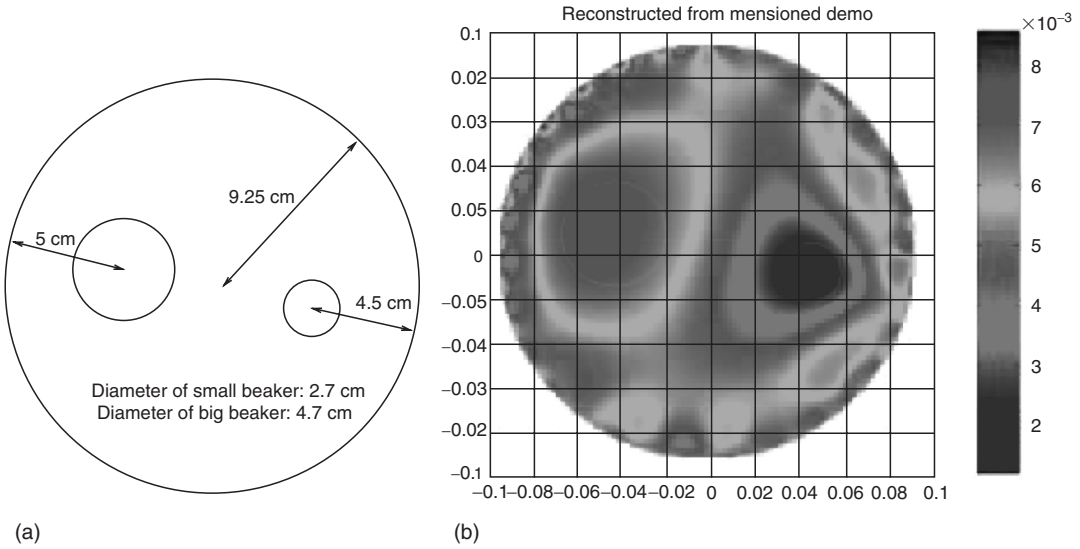

FIGURE 12.12 (See color insert following page 380.)
Left: The setup for Case 3 with one larger metal object and one smaller insulator object. Right: The reconstructed σ. The two circles denote the locations of the objects.

object is a resistive beaker (an insulator). This represents a more interesting case for reconstruction as the conductivity contrast is positive in one region and negative in another.

The reconstructed σ is shown in the right panel of Figure 12.12. The anomalies reconstructed match well with the original objects in location. However, the size of both objects has been somewhat overestimated. The conductivity value of the bigger object is indeed greater than the background, and the smaller object has conductivity values smaller than the background. These indeed match with the original setting that one object is a conductor and another is an insulator, although again the exact values of conductivity are not obtained because of the large contrasts. Nevertheless, the reconstructed images show high-quality reconstruction.

The CPU time for the above image reconstruction examples is less than 3 min on a Pentium IV computer. We emphasize that this speed is expected to be greatly reduced once the program is optimized. Furthermore, in clinical application, the image reconstruction will be performed offline, and thus the computation time of a few minutes is not a concern.

Observations—There are some artifacts in the areas close to the electrodes, perhaps caused by the surface resistance at the interface between the saline solution and the electrodes. However, the overall reconstructed images are excellent. The size and shape of the objects can be well predicted by the reconstructed images. Our future work is to extend the methodology reported here to a full 3-D EIT system. In such a system, we will further improve the sensitivity and resolution of the system by incorporating higher-precision multimeters and by placing a denser 3-D electrode array in the system. Furthermore, to match the higher sensitivity and resolution requirements, we will improve the accuracy of the forward and inverse solvers by incorporating higher-order and spectral methods. From the successful data acquisition and image reconstruction with our 2-D EIT system, it is believed that the 3-D EIT system is highly promising for breast cancer detection.

12.7 Summary and Conclusions

This chapter is a brief summary of MWI and electrical impedance tomography projects ongoing at Duke University. The modeled and measured results presented herein on artificial materials show the kinds of clear images one would fully expect to generate in the clinic using the same techniques. Other research groups are also developing improved MWI and impedance imaging systems, and some breast cancer images derived from clinical data have been published [14,44,45]. Because of 2-D artifacts or algorithm limitations, the earlier clinical images are not as clear as the ones that can be generated with the improved techniques now available. While improvements in current prototypes are encouraging, more work remains before MWI and EIT systems are integrated into clinical applications to produce the high-resolution breast cancer images that are now obtained in the laboratory.

Acknowledgment

We wish to thank the students and postdoctoral research associates involved in the work. Rebecca Willett, Adam Bryan, Erika Ward, Patrick Mathias, John Stang, and Rodger Dalton made significant contributions to the development of MWI hardware. Zhong Qing Zhang helped to develop the forward and inverse scattering algorithms for MWI. Jim Di Sarro, Jackie Hu, Guining Shi, Gang Ye, and Kyle McCarter made significant contributions to the development of electrical impedance tomography hardware. Kim Hwa Lim and Jun Ho Lee developed the forward and inverse solvers for electrical impedance tomography.

References

1. W.T. Joines, R.L. Jirtle, M.D. Rafal, and D.J. Schaefer, ''Microwave power absorption differences in normal and malignant tissue,'' *Int. J. Radiat. Oncol. Biol. Phys*., Vol. 6, No. 6, 681–687, June 1980.
2. W.T. Joines, S. Shrivastav, and R.L. Jirtle, ''A comparison using tissue electrical properties and temperature rise to determine relative absorption of microwave power in malignant tissue,'' *Med. Phys. J*., Vol. 16, No. 3, 840–844, Dec. 1989.
3. R. Pethig, ''Dielectric properties of biological materials,'' *IEEE Trans. Elect. Insul*., Vol. 19, 453–474, 1984.
4. S.S. Chaudhary, R.K. Mishra, A. Swarup, and J.M. Thomas, ''Dielectric properties of normal and malignant human breast tissues at radiowave and microwave frequencies,'' *Indian J. Biochem. Biophys*., Vol. 21, 76–79, 1984.
5. W.T. Joines, ''Frequency dependent absorption of electromagnetic energy in biological tissue,'' *IEEE Trans. Biomed. Eng*., Vol. 31, 215–222, Jan. 1984.
6. W.T. Joines, Y. Zhang, C. Li, and R.L. Jirtle, ''The measured electrical properties of normal and malignant human tissues from 50 to 900 MHz,'' *Med. Phys. J*., Vol. 21, No. 4, 547–550, Apr. 1994.
7. A.M. Campbell and D.V. Land, ''Dielectric properties of female human breast tissue measured at 3.2 GHz,'' *Phys. Med. Biol*., Vol. 37, No. 1, 193–210, June 1992.
8. L. Jofre, M.S. Hawley, A. Broquetas, E. de los Reyes, M. Ferrando, and A.R. Elias-Fuste, ''Medical imaging with a microwave tomographic scanner,'' *IEEE Trans. Biomed. Eng*., Vol. 37, No. 3, 303–312, 1990.

9. Q.H. Liu, Z.Q. Zhang, T. Wang, G. Ybarra, L.W. Nolte, J.A. Bryan, and W.T. Joines, ''Active microwave imaging I: 2-D forward and inverse scattering methods,'' *IEEE Trans. Microwave Theory Technol*., Vol. 50, No. 1, 123–133, Jan. 2002.
10. E.C. Fear, S.C. Hagness, P.M. Meaney, M. Okoniewski, and M.A. Stuchly, ''Enhancing breast tumor detection with near-field imaging,'' *IEEE Microwave Mag*., 48–56, Mar. 2002.
11. P.M. Meaney, K.D. Paulsen, A. Hartov, and R.K. Crane, ''An active microwave imaging system for reconstruction of 2-D electrical property distributions,'' *IEEE Trans. Biomed. Eng*., Vol. 42, No. 10, 1017–1025, 1995.
12. S.C. Hagness, A. Taflove, and J.E. Bridges, ''Two-dimensional FDTD analysis of a pulsed microwave confocal system for breast cancer detection: fixed-focus and antenna-array sensors,'' *IEEE Trans. Biomed. Eng*., Vol. 45, No. 12, 1470–1479, 1998.
13. S.C. Hagness, A. Taflove, and J.E. Bridges, ''Three-dimensional FDTD analysis of a pulsed microwave confocal system for breast cancer detection: design of an antenna-array element,'' *IEEE Trans. Antennas Propagat*., Vol. 47, No. 5, 783–791, 1999.
14. P.M. Meaney, M.W. Fanning, D. Li, P. Poplack, and K.D. Paulsen, ''A clinical prototype for active microwave imaging of the breast,'' *IEEE Trans. Microwave Theory Technol*., Vol. 48, No. 11, 1841–1853, 2000.
15. E.C. Fear and M.A. Stuchly, ''Microwave detection of breast cancer,'' *IEEE Trans. Microwave Theory Tech*., Vol. 48, No. 11, 1854–1863, 2000.
16. Pethig R., *Dielectric and Electronic Properties of Biological Materials*, Wiley, New York, 1979.
17. P. Debye, *Polar Molecules*, Chemical Catalog Co., New York, 1929.
18. R.F. Harrington, *Field Computation by Moment Methods*, Macmillan, New York, 1968.
19. D.E. Livesay and K.M. Chen, ''Electromagnetic fields induced inside arbitrarily shaped biological bodies,'' *IEEE Trans. Microwave Theory Technol*., Vol. 22, 1273–1280, Dec. 1974.
20. D.H. Schaubert, D.R. Wilton, and A.W. Glisson, ''A tetrahedral modeling method for electromagnetic scattering by arbitrarily shaped inhomogeneous dielectric bodies,'' *IEEE Trans. Antennas Propagat*., Vol. 32, 77–85, Jan. 1984.
21. C.T. Tsai, H. Massoudi, C.H. Durney, and M.F. Iskander, ''A procedure for calculating fields inside arbitrarily shaped, inhomogeneous dielectric bodies using linear basis functions with the moment method,'' *IEEE Trans. Microwave Theory Technol*., Vol. 34, 1131–1139, Nov. 1986.
22. H. Massoudi, C.H. Durney, and M.F. Iskander, ''Limitations of the cubical block model of man in calculating SAR distributions,'' *IEEE Trans. Microwave Theory Technol*., Vol. 32, 746–751, Aug. 1984.
23. N.N. Bojarski, ''*k*-Space formulation of the scattering problem in the time domain,'' *J. Acous. Soc. Am*., Vol. 72, 570–584, 1982.
24. T.K. Sarkar, E. Arvas, and S.M. Rao, ''Application of fast Fourier transform and the conjugate gradient method for efficient solution of electromagnetic scattering from both electrically large and small conducting bodies,'' *Electromagnetics*, Vol. 5, 99–122, 1985.
25. H. Gan, and W.C. Chew, ''A discrete BCG-FFT algorithm for solving 3D inhomogeneous scatterer problems,'' *J. Electromagn. Waves Appl*., Vol. 9, 1339–1357, 1995.
26. C. Lanczos, ''An iteration method for the solution of the eigenvalue problem of linear differential and integral operators,'' *J. Res. Nat. Bur. Stand*., Vol. 45, 255–282, 1950.
27. Q.H. Liu, X.M. Xu, B. Tian, and Z.Q. Zhang, ''Applications of nonuniform fast transform algorithms in numerical solutions of differential and integral equations,'' *IEEE Trans. Geosci. Remote Sensing*, Vol. 38, 1551–1560, 2000.
28. Z.Q. Zhang and Q.H. Liu, ''Three-dimensional weak-form conjugate- and bi-conjugate FFT methods for volume integral equations,'' *Microwave Opt. Technol. Lett*., Vol. 5, 350–356, 2001.
29. X. Xu, Q.H. Liu, and Z.Q. Zhang, ''The stabilized biconjugate gradient fast Fourier transform method for electromagnetic scattering.'' *J. Appl. Computat. Electromagn. Soc*., Vol. 17, No. 1, 97–103, Mar. 2002.
30. E. Bleszynski, M. Bleszynski, and J. Jaroszewicz, ''Adaptive integral method for solving large-scale electromagnetic scattering and radiation problems,'' *Radio Sci*., Vol. 31, 1225–1251, 1996.
31. Z.Q. Zhang and Q.H. Liu, ''A volume adaptive integral method (VAIM) for 3D inhomogeneous objects,'' *IEEE Antennas Wireless Propagat. Lett*., Vol. 1, No. 6, 102–105, 2002.
32. Z.Q. Zhang, Q.H. Liu, and X.M. Xu, ''RCS computation of large inhomogeneous objects using a fast integral equation solver,'' *IEEE Trans. Antennas Propagat*., Vol. 51, No. 3, 613–618, Mar. 2003.

33. Z.Q. Zhang, and Q.H. Liu, ''Two nonlinear inverse methods for electromagnetic induction measurements,'' *IEEE Trans. Geosci. Remote Sensing*, Vol. 39, No. 6, 1331–1339, June 2001.
34. Z.Q. Zhang, Q.H. Liu, C. Xiao, E. Ward, G. Ybarra, and W.T. Joines, ''Microwave breast imaging: 3-D forward scattering simulation,'' *IEEE Trans. Biomed. Eng.*, Vol. 50, No. 10, 1180–1189, Oct. 2003.
35. Z.Q. Zhang and Q.H. Liu, ''3-D nonlinear image reconstruction for microwave biomedical imaging,'' *IEEE Trans. Biomed. Eng.*, Vol. 51, No. 3, 544–548, 2004.
36. L.E. Baker, ''Principles of the impedance technique,'' *IEEE Eng. Med. Biol. Mag.*, 11–15, Mar. 1989.
37. S. Caorsi, G.L. Gragnani, and M. Pastorino, ''Redundant electromagnetic data for microwave imaging of three-dimensional dielectric objects,'' *IEEE Trans. Antennas Propagat.*, Vol. 42, No. 5, 581–589, May 1994.
38. M. Cheney and D. Isaacson, ''Distinguishability in impedance imaging,'' *IEEE Trans. Biomed. Eng.*, Vol. 39, No. 8, 852–860, Aug. 1992.
39. B.M. Eyuboglu, B.H. Brown, and D.C. Barber, ''*In vivo* imaging of cardiac related impedances changes,'' *IEEE Eng. Med. Biol. Mag.*, 39–45, Mar. 1989.
40. A.D. Seagar, D.C. Barber, and B.H. Brown, ''Electrical impedance imaging,'' *IEEE Proc.*, Vol. 134, Pt. A, 201–210, 1987.
41. W.T. Joines, E. Tanabe, and Raymond U, ''Determining the electrical properties of biological tissue *in vivo*,'' *IEEE Proc. Southeast. Conf.*, 382–385, Apr. 1976.
42. W.C. Chew, *Waves and Fields in Inhomogeneous Media*, Van Nostrand Reinhold, New York, 1990.
43. Q.H. Liu, ''Nonlinear inversion of electrode-type resistivity measurements,'' *IEEE Trans. Geosci. Remote Sensing*, Vol. 32, No. 3, 499–507, 1994.
44. T.E. Kerner, K.D. Paulsen, A. Hartov, S.K. Soho, and S.P. Poplack, ''Electrical impedance spectroscopy of the breast: clinical imaging results in 26 subjects,'' *IEEE Trans. Med. Imaging*, Vol. 21, No. 6, 638–645, June 2002.
45. A. Malich, T. Fritsch, R. Anderson, T. Boehm, M.G. Freesmeyer, M. Fleck, and W.A. Kaiser, ''Electrical impedance scanning for classifying suspicious breast lesions: first results,'' *Eur. Radiol.*, Vol. 10, No. 10, 1555–1561, 2000.